Journal of Colloid and Interface Science 655 (2024) 886–898

Contents lists available at ScienceDirect

Journal of Colloid And Interface Science

journal homepage: www.elsevier.com/locate/jcis

Addressing the synchronized impact of a novel strontium titanium over copolymerized carbon nitride for proficient solar-driven hydrogen evolution

Zeeshan Ajmal [a,b,1], Mahmood Ul Haq [a,1], Shahid Zaman [c], M.K. Al-Muhanna [d], Anuj Kumar [e], Mohammed M. Fadhali [f], Siwar Ben Hadj Hassine [g], Muhammas Qasim [h], K.F. Alshammari [i], Ghulam Abbas Ashraf [j,k,*], Abdul Qadeer [l,*], Adil Murtaza [m,*], Sulaiman Al-Sulaimi [n,*], Huaqiang Zeng [b,*]

[a] Key Laboratory of the Ministry of Education for Advanced Catalysis Materials, Institute of Advanced Fluorine-Containing Materials, College of Chemistry and Material Science, Zhejiang Normal University, Jinhua 321004, Zhejiang, China
[b] School of Chemistry and Chemical Engineering, Northwestern Polytechnical University, 710072 Xian, China
[c] Institut d'Innovations en Écomatériaux, Écoproduits et Écoénergies, Université du Québec à Trois-Rivières (UQTR), 3351 boul. des forges, Trois-Rivières, Québec G8Z 4M3, Canada
[d] The Material Science Research Institute, King Abdulaziz City for Science and Technology (KACST), Riyadh 11442, Saudi Arabia
[e] Nanotechnology Research Laboratory, GLA, University, Mathura, Uttar Pradesh 281406, India
[f] Department of Physics, Faculty of Science, Jazan University, Jazan 45142, Saudi Arabia
[g] Department of Computer Science, College of Science and Arts at Muhayel, King Khalid University, Saudi Arabia
[h] School of Electronic Engineering, Jiujiang University, Jiujiang 332005, China
[i] Department of Criminal Justice and Forensics, King Fahad Security College, Riyadh 11461, Saudi Arabia
[j] College of Environment, Hohai University, Nanjing 210098, China
[k] New Uzbekistan University, Mustaqillik Ave. 54, Tashkent 100007, Uzbekistan
[l] State Key Laboratory of Environmental Criteria and Risk Assessment, Chinese Research Academy of Environmental Science, Beijing, China
[m] MOE Key Laboratory for Non-equilibrium Synthesis and Modulation of Condensed Matter, State Key Laboratory for Mechanical Behaviour of Materials, Key Laboratory of Advanced Functional Materials and Mesoscopic Physics of Shaanxi Province, School of Physics, Xian Jiaotong University, 710049 Xian, Shaanxi, China
[n] Department of Biological Science and Chemistry, University of Nizwa, Oman

GRAPHICAL ABSTRACT

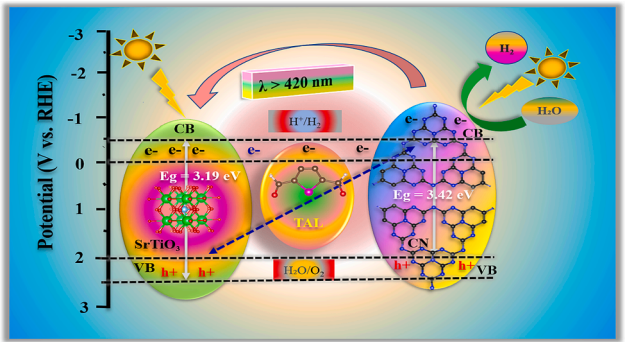

* Corresponding authors.
E-mail addresses: zeeshan@nwpu.edu.cn, zisheuaf@gmail.com (Z. Ajmal), ga_phy@yahoo.com (G.A. Ashraf), adilmurtaza91@mail.xjtu.edu.cn (A. Murtaza), s.salimi@unizwa.edu.om (S. Al-Sulaimi), hzeng@fzu.edu.cn (H. Zeng).
[1] Zeeshan Ajmal & Mahmood Ul Haq contributed equally to this work.

https://doi.org/10.1016/j.jcis.2023.10.020
Received 26 April 2023; Received in revised form 1 October 2023; Accepted 5 October 2023
Available online 9 October 2023

ARTICLE INFO

Keywords:
Carbon nitride
Thiophenedicarboxyl
Strontium-titanium
Heterojunction
Photocatalytic hydrogen evolution
Copolymerization

ABSTRACT

Currently, novel technologies are highly prerequisite as an outstanding approach in the field of photocatalytic water splitting (PWS). Previous research has shown that copolymerization technology could improve the photocatalytic performance of pristine carbon nitride (CN) more efficiently. As this technology further allows the charge carrier recombination constraints, due to novel monomer-incorporated highly abundant surface-active sites of metals in polymeric carbon nitride-based heterojunction. However, in present study, a novel previously unexplored thiophenedicarboxaldehyde (TAL) conjugated, strontium-titanium ($SrTiO_3$) induced and CN based heterojunction, i.e., $SrTiO_3$/CN-$TAL_{10.0}$, was prepared for solar-driven hydrogen evolution reaction (HER). This heterojunction effectively enables the proficient isolation of photoinduced charge carriers and enhanced the charge transport over the surface junction, by enhancing the optical absorption range and average lifetime of photogenerated charges. The incorporation of TAL within the structure of CN via copolymerization highly increases the photocatalytic activity, as well as maintaining its photostability performance. The $SrTiO_3$ concentration and the proportion of TAL among CN can be precisely controlled to provide the optimal photocatalytic efficiency with a maximum HER of 285.9 μmol/h under visible light (λ = 420 nm). Based on these results, our optical analysis shows that coupling of $SrTiO_3$ and TAL monomer in the structure of CN considerably reduce the band gap of superior sample from (3.42 to 2.66 eV), thereby, signifying the outstanding photocatalytic performance of $SrTiO_3$/CN-$TAL_{10.0}$. Thus, this study provide a new guideline in order to develop the multidimensional photocatalysts with proper functioning for sustainable energy conversion and production.

1. Introduction

The rapid depletion of fossil fuel and environmental pollution originated from different industrial and anthropogenic activities have become a serious problem in future energy supply and global climate change [1-4]. These things are actually motivating the researchers to develop new sustainable energy generation technology [5,6]. The most prevalent reduction technologies or processes, such as carbon reduction reaction [7,8], water splitting reaction [9,10], nitrogen reduction reaction [11,12], and, oxygen reduction reaction [13,14], might successfully address such growing energy problems, while also reducing the environmental pollution [15-18]. Photocatalytic water splitting particularly in the form of hydrogen (H_2) energy is regarded as a promising pathway in order to solve the existing energy shortage issue. However, photocatalytic technology could simulate the natural process of photosynthesis in order to convert the solar energy into direct chemical energy, by offering a reliable solution for sustainable energy generation as well as environmental detoxification processes [19-23]. However, the primary considerations to address the use of this technology at feasible level are the visible light driven better efficiency, affordability of photocatalysts, and its stability [24-28]. However, there are numerous factors, which may affect the photocatalytic water splitting more effectively such as the production of exciton upon light absorptions [29,30], redox potential, quick parting of charges, and their migration to approach suitable CB and VB edge positions [31,32]. More importantly, high-quantum-value semiconductors are more advantageous for solar energy, because they absorb visible light effectively, resulting in photoinduced electrons and hole pairs [25,33]. Therefore, considerable research work were carried out with the aim of improving energy conversion performance of semiconductor-based photocatalysts including $NaMO_3$ (M = Nb and Ta) [34], $PbMoO_4$ [35], ZnO/ZnS or Cds [36,37], TiO_2 [38,39], $SrTiO_3$ [40], g-C_3N_4 [10,41-44], and photocatalysts doped with metal cations [45,46].

Recently, metal-free two-dimensional (2D) graphitic carbon nitride (CN) have received much interest in different research fields, due to outstanding chemical stability, high surface area, high redox ability, and appropriate band gap (Eg = 2.7 eV), conduction band (CB) of 0.8 V and valence band (VB) of 1.9 V vs. RHE [10,47,48]. However, the low efficiency of bulk CN renders it inappropriateness for photocatalytic application. It is mainly due to large band gap, which showed its poor visible-light harvesting capacity rapid charge recombination, minimal quantum yield, low crystallinity, and low surface area [49]. The development of highly promising photocatalytic system highly needed the efficient use of a wide range of hosts surface modification techniques, each of which has a significant impact on either the adsorption/activation ability of reaction molecules or the effectiveness of charge carrier movement. Moreover, the organic ligand integration via molecular engineering within the CN framework has emerged as an intriguing strategy for reducing the recombination of charges with fast separation and their subsequent movement, thereby, enhancing its photocatalytic activity under visible light [24,50-52]. However, a wide range of monomer induced visible light driven CN (380–750 nm) with remarkable photocatalytic water splitting (PWS) activities has already been proposed [53,54]. In this aspect, a large number of studies have been done to synthesize monomer induced (donor-acceptor) CN, those have much higher PWS catalytic activity than simple CN. Despite growing interests regarding the extensive use of organic ligands for PWS, the little improvements further need highly efficient organic monomers for wonderful results. As a result, combining organic ligand-induced carbon-based CN with transition metal strontium-titanium ($SrTiO_3$) (e.g., $SrTiO_3$/CN-$TAL_{10.0}$) might effectively overcome the inherent shortcomings associated with these materials. As, it has been shown that pristine CN, TiO_2, and $SrTiO_3$ in the form of a single semiconductor cannot experience the usual PWS. However, the use of $SrTiO_3$ has recently received a much attention in photocatalysis, due to its interesting structural, chemical, and physical properties [55,56]. In addition, $SrTiO_3$ has the delocalized characteristics of photoexcited electrons and suitable band edge position, which play an important role to enhance its efficacy towards photocatalytic applications. However, the $SrTiO_3$ is only capable of absorbing the UV light specifically owing to intrinsic large bandgap energy (E_g = 3.2 eV) [57]. To alter the electronic bandgap of $SrTiO_3$ to confirm its efficient working capacity under visible light, a lot of metals and non-metals doping methods have been used [58,59]. However, it is noteworthy that metal doping technique could easily produce phase impurity, which could further act as a main centre of electron hole pairs recombination. Hence, non-metal doping strategy in order to properly tune the crystal structure of $SrTiO_3$ by making it more efficient under visible light irradiation has become an attractive alternative approach [60]. In this context, many strategies have been continuously followed for the designing and proper tuning of $SrTiO_3$ as a valuable photocatalyst under visible light. The direct heterojunction strategy via combining two semiconductors has been viewed as an effective approach by increasing the charge carrier's separation efficiency and consequently increased the photocatalytic performance of photocatalyst [61,62]. However, type-II heterojunction with staggered bandgap has been proved as an effective way owing to a promising characteristic of forming an efficient interface junction. Moreover, that is the most prevailing energy gradient over the interfaces to spatially

separate the charge carriers over the different edges/locations of heterojunction, wherein the electrons could be localized at one side and the holes towards other side [63]. These spatially confined electrons along with holes in type-II heterojunction could effectively make them highly appropriate materials for an efficient photocatalytic process. Consequently, the organic ligand induced $SrTiO_3$/CN-TAL_x as a typical type-II heterojunction could effectively overcome these problems by enhancing the PWS [64].

In this work we initially prepared the mixing of aromatic π-conjugated monomer, with thiophenedicarboxaldehyde (TAL), in CN framework via a molecular engineering (CN-TAL_x). This modulation demonstrated a nucleophilic substitution reaction and provided an effective intramolecular TAL system for an efficient PWS. During this process, the TAL monomer with a triazine structure functioned as an electron donor-acceptor, resulting in a type of D-π-A photocatalyst for a high photocatalytic performance of water reduction (H_2) process. Similarly, to further increase the electron isolations and improve the photocatalytic H_2 evolution activity, we constructed a multi-junction photocatalyst of $SrTiO_3$ embedded within pristine CN and copolymerized CN (CN-TAL_x). The as-synthesized heterojunction ($SrTiO_3$/CN-$TAL_{10.0}$) demonstrated substantial visible light selectivity, as well as extremely effective charge transport isolation and transition, which was extremely beneficial for its elevated behavior in H_2 generation. Importantly, the high stability of the $SrTiO_3$/CN-$TAL_{10.0}$ heterojunction for H_2 generation, along with the physicochemical, optical, electronic properties and the photocatalytic mechanism of $SrTiO_3$/CN-$TAL_{10.0}$ has been presented for the first time in detail.

2. Material and methods

2.1. Materials

All chemicals are of high grade and were being used without further purification. Hydrated Strontium nitrate ($SrNO_3)_2$, 99%, Sigma Aldrich, purity: 98%), urea (Sigma Aldrich, purity: 98 percent), Et–OH (C_2H_5OH, 99%), TiO_2 ((P25), Sigma Aldrich), Sulfuric acid mixture (H_2SO_4, Sigma Aldrich), thiophenedicarboxaldehyde (TAL), (Sigma Aldrich, purity: 99.9%), chloroplatinic acid ($H_2PtCl_6{\cdot}6H_2O$, Pt 37.5%), metallic silver (Ag), glycerol, triethanolamine (>78%), lactic acid, acetic acid, methanol, lanthanum oxide La_2O_3, silver nitrate ($AgNO_3$) and iron nitrate ($FeNO_3$) were purchased from Adams Chemicals Co. Ltd. (China).

2.2. Material synthesis

2.2.1. Synthesis of CN photocatalyst

The CN was prepared by selecting urea as a major precursor. For that (10 g) urea was dispersed in 60 mL water. Thereafter, solution was continuously stirred at 90 °C, to completely evaporate the water. Afterward, as-obtained product was shifted into crucible, for calcination at 550 °C with increasing temperature ramp rate of 2.3 °C min^{-1} for 2 h. The final pale-yellow powder was completely crushed into fine powder, and then clearly washed with deionized water and ethanol, then kept into oven for drying at 80 °C. The final product was named as CN.

2.2.2. Synthesis of copolymerized CN-TAL_x photocatalyst

The copolymerized CN-TAL_x was synthesized by the same process as mentioned above for CN synthesis. In a given procedure, different concentrations of TAL monomer (i.e., 5.0, 10.0 and 20.0 mg) were mixed with 10 g of urea through the molecular engineering (copolymerization process). The parental solution was treated under oil bath system by mechanical stirring at 90 °C, to completely evaporate the water. The resultant final products were named CN-$TAL_{5.0}$, CN-$TAL_{10.0}$, and CN-$TAL_{20.0}$, correspondingly. After trial experiment, the 10.0 mg of TAL was chosen as the ideal quantity to be incorporated inside the skeleton of CN to provide the highest photocatalytic performance. Therefore, we kept the amount of TAL as constant with fixed amount of 10 mg within CN photocatalyst such as CN-$TAL_{10.0}$ for further process.

2.2.3. Synthesis of $SrTiO_3$ photocatalyst

The $SrTiO_3$ was prepared via one-pot hydrothermal pathway by a slightly modified procedure [65]. Specific amount of TiO_2 (P25) was mixed with an $(SrNO_3)_2$ in 50 mL of deionized water and left for stirring for 1 h to get a homogeneous suspension (adsorption–desorption). Moreover, 3 mL NaOH solution was added to the solution, and the pH of solution was adjusted at 13.0. The solution was then transferred into a 100 mL stainless steel lined sealed autoclave and heated at 200 °C for 4 h. After hydrothermal process, the mixture was separated from the reaction solution by centrifugation and washed repeatedly with HCl and DI water. Finally, the resultant material was dried in a vacuum oven at 80 °C and the final product was named as $SrTiO_3$.

2.2.4. Synthesis of $SrTiO_3$/CN-$TAL_{10.0}$ heterojunction

The $SrTiO_3$/CN-$TAL_{10.0}$, was synthesized by using (pristine $SrTiO_3$ and copolymerized CN-$TAL_{10.0}$). The specific quantity of each catalyst was dissolved in a 50 mL of deionized water and reaction was left for stirring for 2 h to completely mix the both catalysts. Then solution was centrifuged and 3 times washed with water and ethanol. Lastly, sample was placed in oven for drying at 70 °C. By adopting the same procedure discussed for $SrTiO_3$/CN-$TAL_{10.0}$ material, the $SrTiO_3$/CN, photocatalyst was prepared by simply mixing the pristine $SrTiO_3$ and pristine CN.

2.2.5. Density functional theory (DFT) calculations

In present work, spin-polarized density-functional-theory (DFT) simulations were carried out with the help of Quantum Espresso program using Gaussian 09 software [66]. The Electronic density of states (DOS) and the bands of $SrTiO_3$/CN material were determined using a projector augmented-wave (PAW) potential and the generalized gradient approximation (GGA) of the Perdew-Burke-Ernzerhof (PBE) functional terms. The plane-wave expansion of the electronic wave function was performed using a 250-eV energy cut off, and the convergence thresholds for force and energy were set to 0.05 eV^{-1} and 10–5 eV, respectively. For the first Brillouin region, we used the Monkhorst-Pack sampling method on a 1 × 3 × 1 k-point grid with the gamma points at the centre [67,68]. As part of the slab model development process, a vacuum zone 15 above the slab's surface was added into the periodic boundary condition (PBC). Monoclinic surface of as-prepared materials was modelled, and a (2 × 2) supercell was constructed to represent it. When it came to energy and force convergence, slab models allowed the atomic locations to become entirely relaxed [69].

2.2.6. Characterization

The materials characterization like structural, optical, and morphological properties were investigated by different analytical characterization machines. The X-ray diffraction (XRD) spectra was measured by using an advanced Bruker D8 diffractometer at 40 mA with Cu alpha irradiation at 40 Kv. The XPS spectra was examined on Thermo ESCALAB250 X-ray photoelectron spectroscopy (XPS) with monochromatized Al Ka line source (200 W). The FTIR spectra was recorded on Bruker 70 Vertex Infrared Spectroscopy. Similarly, the surface area characteristics with pore volume were investigated using Micromeritics TriStar 3000 system. All the UV-DRS spectra were recorded on a Hitachi model UV-DRS-4100 UV–vis spectrophotometer using barium sulfate as references. The Photoluminescence (PL) spectra were done on an Edinburgh FI/FSTCSPC 920 spectrophotometer. The electron paramagnetic resonance (EPR) spectra were done on an instrument of Bruker model A300 spectrometer. Furthermore, the sample morphology and particle size were visualized using Transmission electron microscopy (TEM) of JEOL model 2100 Plus and field emission scanning electron microscope (FE-SEM) Hitachi New Generation SU8010. The Raman experiments were performed on Renishaw Vi-Reflex spectroscopy.

2.2.7. Photocatalytic hydrogen (H_2) evolution test

The PWS for H_2 evolution was performed in a Pyrex top-irradiation reaction vessel, having closed glass gas circulation with an evacuation system connected with a 300 W-Xe lamp. In each cycle, the specific amount of photocatalyst (50 mg) was added into 100 mL of water with 10 vol% triethanolamine (TEOA) solution as a sacrificial agent, and Pt as a co-catalyst (3 wt%). Then suspension was vacuumed for 30 min and irradiated the reaction system using a Xenon lamp (PLS-SXE 300/300UV, Beijing Perfect light Technology Co. Ltd, China) with a UV cut-off filter ($\lambda > 420$ nm) to eliminate UV and IR light. A circulated water system was connected to the main setup to keep the temperature of the reaction at 283 K. After the completion of the photocatalytic reaction at an appropriate time, the as-produced gases were analysed using gas chromatography (GC), which was equipped with a thermal conductive detector and a molecular sieve column of 5 Å for evaluation of H_2 gas. The argon (Ar) gas was used as a carrier gas to push gases from system to GC. For a long durability test, the system was allowed for 5 catalytic cycles over 25 h and evacuated after each cycle, respectively.

2.2.8. Electrochemical measurement

The electrochemical experiment was performed using the BioLogic VSP-300 electrochemical analyse system having three conventional electrodes. About 1 M of potassium hydroxide (KOH) solution was used as the supporting electrolyte. During measurement, as-synthesized materials (photocatalysts) was used as working electrode, along with Ag/AgCl (as a reference electrode) and Pt wire (as a counter electrode). The 300 W Xenon lamp was used as light source. The electrochemical impedance spectroscopy (EIS) measurement of CN, CN-$TAL_{10.0}$ and $SrTiO_3$/CN-$TAL_{10.0}$ were conducted in 50 mL of 1 M KOH aqueous solution at −0.4 V vs. Ag/AgCl electrode in dark. The working electrode in photocurrent experiment, was irradiated to minimize the thickness effect of semiconductor layer and periodic on/off photocurrent response of CN, CN-$TAL_{10.0}$ and $SrTiO_3$/CN-$TAL_{10.0}$ modified FTO, and perturbation signal was also 20 mV.

3. Result and discussion

All samples were characterized using X-ray Powder Diffraction (XRD) to understand the phase composition (Fig. 1**a**). The two main peaks at 13.1° and 27.6° were observed in the spectra of pure CN, CN-TAL_x (x = 5.0, 10.0, and 20.0), and $SrTiO_3$/CN materials, showing the corresponding formation of crystal structure. The analogous small peak at 13.1° is assigned to 100 planes, illustrating to the packing motif of tris-triazaine in-construct structural planes, while the peak at 27.6° assigned to 002 planes, therefore depicting the inter-planar assembly of conjugated aromatic structure. After increasing the quantity of TAL, a slight increase in the magnitude of the 0 0 2 peak was observed. Similarly, a distinctive peak at around 27.2° for the $SrTiO_3$/CN composites has been analysed [70]. The XRD pattern of $SrTiO_3$ demonstrated several strong peaks at 2ɵ = 32.47, 40.01, 44.82, 59.32, 63.74, and 76.93, which can be designated to the planes of (1 1 0), (1 1 1), (2 0 0), (2 1 1), (2 2 0), and (3 1 0) that correspond to the cubic structure of as-synthesized pure $SrTiO_3$ (JCPDS card no.: 74–1296). Besides, some extra peaks at 2θ = 33.11°, 40.03°, 44.97°, 58.17°, and 64.97° appeared in $SrTiO_3$/CN-$TAL_{10.0}$. These peaks are assigned to the diverse crystal planes of cubic $SrTiO_3$ (PDF #35-0734). They include 110, 111, 200, 211, and 220 planes, respectively [71]. Similarly, Fourier transform infrared spectroscopy (FTIR) of all sample were collected to determine the surface functional groups of different peaks at distinct positions. In CN and copolymerized CN-TAL_x, a systematically arranged series of bands were noticed from 1200 to 1700 cm^{-1}, which were attributed to the stretching of bands i.e., C(sp^2)-N and C(sp^2) = N in the CN. A main distinctive bending position in CN was noticed at 810 cm^{-1}, which is the typical representative of s-triazine subunit. Moreover, a distinctive broad band, and some of the suppressed peaks within the range of 3000–3600 cm^{-1} are ascribed to N—H stretching, thus, verifying the existence of NH or/and NH_2 groups on the surface sites of materials (Fig. 1**b**). In addition, it was more apparent that CN-TAL_x catalysts exhibited sharp FTIR peaks than CN catalysts due to the extraordinary growth, which is entirely associated with a valuable, pristine surface structure with a vastly expanded surface area. The FTIR analysis of superior sample $SrTiO_3$/CN-$TAL_{10.0}$ demonstrated major peaks observed at 597, 801, 1231, 1384, 1467, 1575, 1683, and 3287 cm^{-1}, signifying the presence of different surface functional groups such as Sr–O or Ti–O, C—O, C—N, C—C, C═N, CH (asymmetrical), and N—H groups [72,73]. Another obvious peak was noticed in $SrTiO_3$/CN at 555 cm^{-1}, which is attributed to the UV distinctive vibrations of $SrTiO_3$ and therefore a strong peak at 643 cm^{-1} demonstrates the Ti–O stretching vibrations. Similarly an intense peak at 1511 cm^{-1} in $SrTiO_3$ indicates the presence of N—O species [74]. The textural parameters of as-prepared samples were further investigated in terms of N_2 adsorption and desorption isotherms (**Table. S1**). Likewise, the CN samples showed calculated specific surface area about 39.4 m^2g^{-1}, which further increased up to 257.3 m^2g^{-1} after the integration of TAL within the matrix of CN. The surface area also substantially increased up to 428.6 m^2/g for $SrTiO_3$/CN-$TAL_{10.0}$ with respect to those of pristine $SrTiO_3$ (64.8 m^2/g), CN (39.4 m^2/g), and CN-$TAL_{10.0}$ (257.3 m^2/g), and showing an adequate space for the interaction of photoinduced electrons and holes upon excitation. The specific BET surface areas (39–428 m^2/g) were considerably increased with average pore volumes (0.19–0.67 cm^3g^{-1}). Furthermore, the C/N molar ratios of as-synthesized material reveal the considerable rises in C/N molar ratio in the range of 0.64 to 0.71 for CN vs $SrTiO_3$/CN-$TAL_{10.\ 0}$ (Fig. 1**c**). In addition, the electronic band structure of materials such as electron paramagnetic resonances (EPR) technique show one solitary Lorentzian stripe 3520 G under dark and visible light at normal room temperature, which has a g value of 2.0034 (Fig. 1**d**). This quantity is closely related to the accumulation of unpaired carbon electrons of π-bonded aromatics at the surface sites of catalysts. More importantly, the EPR signal intensity has dramatically increased with the progressive incorporation of TAL and $SrTiO_3$ guests into the CN framework. The photoluminescence (PL) spectra of all materials revealed an effective fluctuation in the direction of longer wavelengths than that of CN [75]. Such fluctuation in the Pl spectra is caused by reduced electron localization in $SrTiO_3$/CN-$TAL_{10.0}$ and holes in the CN band region, which are initiated due to band offsets and hence prolong the π-conjugation (Fig. 2**a**). Furthermore, the optical absorption edge of TAL-modified CN samples was appeared in the direction of red-shifted, and it showed a strong blend after the impregnation of $SrTiO_3$ with CN-TALx (435–470 nm), which might be due to n–π* transition state. The optical absorption edge of pristine CN was found to be 435 nm, which is assigned to the as π–π* interaction of transition state. In the meantime, the sequential transition in $SrTiO_3$/CN-$TAL_{10.0}$ sample is attributed to its apparent change in colour from pale yellow to dark brown. These considerable variations improvement in light adsorption rate is obviously linked with lower band gap. However, the $SrTiO_3$/CN-$TAL_{10.0}$ samples are considered as promising photocatalysts, owing to a notable development in its optical absorption phenomenon, lowering of bandgap and isolation of electrons and holes followed by their transportation under visible light. The UV–vis Diffuse Reflectance Spectroscopy (DRS) analysis are basically conducted to confirm the fundamental inner structural variations in physicochemical and optical properties of CN, after being de-convolution of organic monomer TAL and semiconductor $SrTiO_3$ within CN (Fig. 2**b**). The findings demonstrate that all photocatalysts exhibit considerable optical adsorption. For pure CN, the absorption bands are visible at 377 nm. Lastly, these absorption band phenomena play a significant role in the photocatalytic activity, because of the excitation of charges from the valence band (VB) to conduction band (CB) of the CN under illumination. This optical absorption of modified materials has been drastically shifted towards a large region of adsorption, similar to the absorption band phenomenon. However, the $SrTiO_3$/CN-$TAL_{10.0}$ display outstanding optical absorption area of 483 nm as compared to other samples. Such modification further leads to a

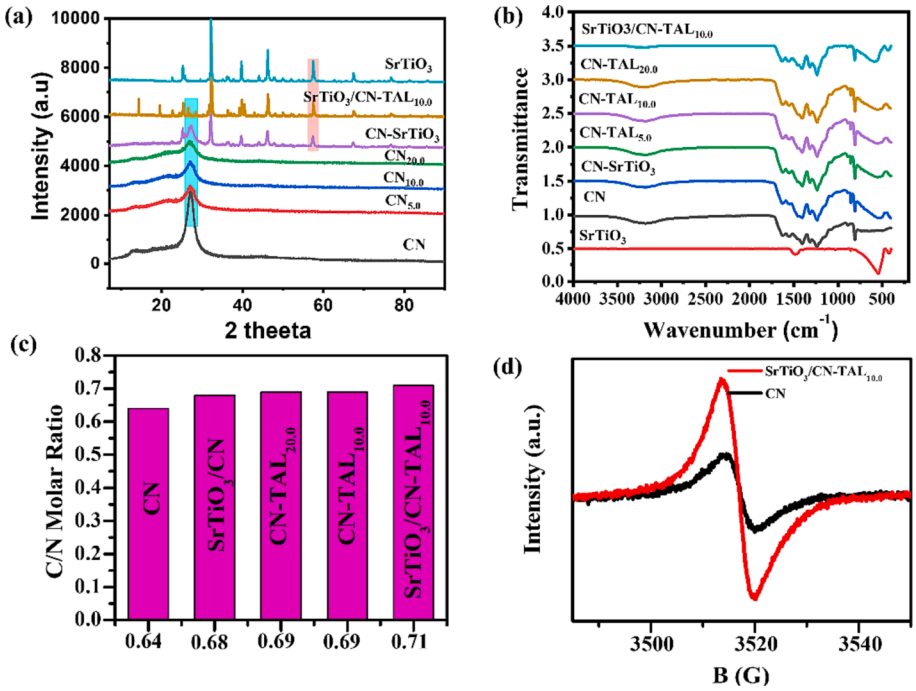

Fig. 1. **(a)** X ray powder diffraction (XRD) and **(b)** Fourier-transform infrared spectroscopy (FTIR) spectra of all samples, **(c)** C/N molar ratios and **(d)** electron paramagnetic resonance (EPR).

consistent reduction in the band gap from 3.39 to 2.65 eV for $SrTiO_3$/CN-$TAL_{10.0}$. The lowered band gap and red shifting of emission spectra lead to a strong integrated consequence and electron transition minimum energy, resulting in intrinsic absorption shifting of $SrTiO_3$/CN-$TAL_{10.0}$.

Therefore, the $SrTiO_3$/CN-$TAL_{10.0}$ samples could be taken as a promising photocatalyst, which is closely associated with the noteworthy progress in its optical absorption phenomenon, by lowering the sample bandgap and recombination of electrons and holes followed by their transportation under visible light for photocatalytic HER [76,77]. Similarly, the band gaps of all synthesized samples were manifested in Table S1. The photo/electrochemical measurement was performed for all samples to determine the charge generation, separation and their further migration over the interface of concerned samples. A considerable increase in the photocurrent intensity was observed in case of CN sample after the integration of TAL. Similarly, the photocurrent intensity

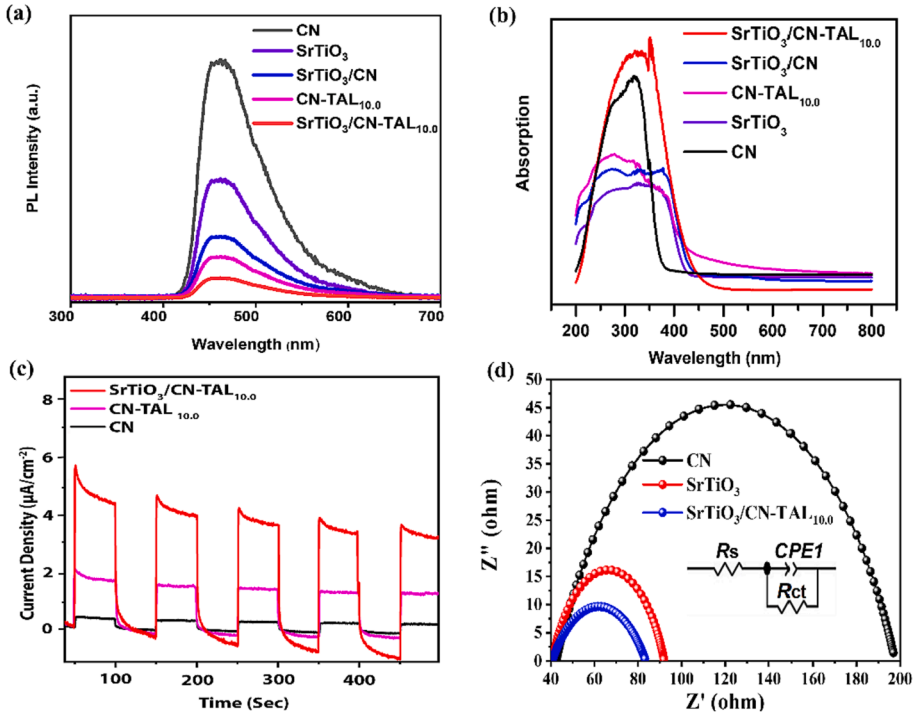

Fig. 2. **(a)** Photoluminescence (PL) spectra **(b)** diffuse reflectance spectroscopy (DRS) spectra of all synthesized photocatalysts as well as **(c)** photocurrent and **(d)** Nyquist plots of CN, CN-$TAL_{10.0}$ and $SrTiO_3$/CN-$TAL_{10.0}$.

of heterojunction sample was further enhanced via doping with $SrTiO_3$ (Fig. 2**c**). Furthermore, the utilization of electrochemical impedance spectroscopy was conducted to elucidate the intricate interfacial charge transfer processes in the catalysts. These processes were subsequently quantified through the analysis of Nyquist plots, as depicted in Fig. 2**d**. Among all the catalysts measured in this study, the $SrTiO_3$/CN-$TAL_{10.0}$ variant displayed the lowest magnitude of charge-transfer resistance (Rct = 43 Ω) according to the data presented in **Table S2**. This distinct characteristic is directly associated with its notably accelerated photocatalytic kinetics. Additionally, a discernible reduction in the semicircular Nyquist plot was observed for both CN-$TAL_{10.0}$ and $SrTiO_3$/CN-$TAL_{10.0}$ in comparison to the CN sample. This distinct variation serves as clear evidence thus, suggesting the synergistic integration of the TAL comonomer and $SrTiO_3$ within the CN framework. This integration has emerged as a pivotal factor substantiating the marked enhancement in the facilitation of photoexcited processes, attributable to the heightened electronic conductivity and superior charge separation efficiency produced by the incorporation of TAL and $SrTiO_3$ within the CN matrix.

The textural and morphological analyses of materials were carried out through Scanning Electron Microscopy (SEM) and Transmission Electron Microscopy (TEM) images as presented in Fig. 3**.** The TEM pictures of CN and copolymerized CN-$TAL_{10.0}$ could be simply distinguished from modified samples with a sheet type structure, while those of $SrTiO_3$ particles are spherical in nature, and therefore, these spherical shaped particles are uniformly distributed over the CN sheet for $SrTiO_3$/CN-TAL materials (Fig. 3**a-d**). Similarly, the TEM morphology for CN was observed with asymmetrical scales by showing nano-sheets (Fig. 3**e**), which was categorized to be prominently divergent from other characterized CN-modified samples (e.g., $SrTiO_3$, CN-$TAL_{10.0}$, and $SrTiO_3$/CN-$TAL_{10.0}$). The $SrTiO_3$ seems to form tiny particles, and the aggregation of these tiny particles having white elongates in more compact structure was observed in case of $SrTiO_3$/CN-$TAL_{10.0}$ with considerably irregular morphology (Fig. 3**f-g**). The mapping study of the $SrTiO_3$/CN-$TAL_{10.0}$ sample via energy-dispersive X-ray spectroscopy (EDS) further confirms the occurrence of all the essential elements such as Sr, Ti, O, N, and C in composite (Fig. 3**i-n**).

In order to gain deeper insight into the interfacial electronic structures, we used the x-ray-photoelectron spectroscopy (XPS) technology which in turn basically provides the bonding configuration of CN and $SrTiO_3$/CN-$TAL_{10.0}$ composites. The XPS survey of the CN, and $SrTiO_3$/CN-$TAL_{10.0}$ samples is presented in Fig. 4**a, i**. From XPS spectra of $SrTiO_3$/CN-$TAL_{10.0}$ sample, the bands ascribed to C, N, Sr, O and Ti elements were clearly noticed, whereas C, N and O were present in pristine CN only. In Sr fitting peak (Fig. 4**b**) in $SrTiO_3$/CN-$TAL_{10.0}$ sample, distinctive peaks at 134.1 eV and 135.9 eV are assigned to 3d5/2 and 3d3/2 core level of Sr^{2+}. The binding energies of Sr peaks in $SrTiO_3$/CN-$TAL_{10.0}$ are relatively smaller, so electron transfer from this heterojunction could be utilized to produce greater effects. The Fig. 4**c** presents the Ti 2p core-level spectra of $SrTiO_3$/CN-$TAL_{10.0}$ indexed at 461.2 and 465.1 eV, which is basically generated due to transition of electron transfer from CN-TAL to $SrTiO_3$. When this heterojunction linked, the positively charged area in CN-$TAL_{10.0}$, increase the binding energy of

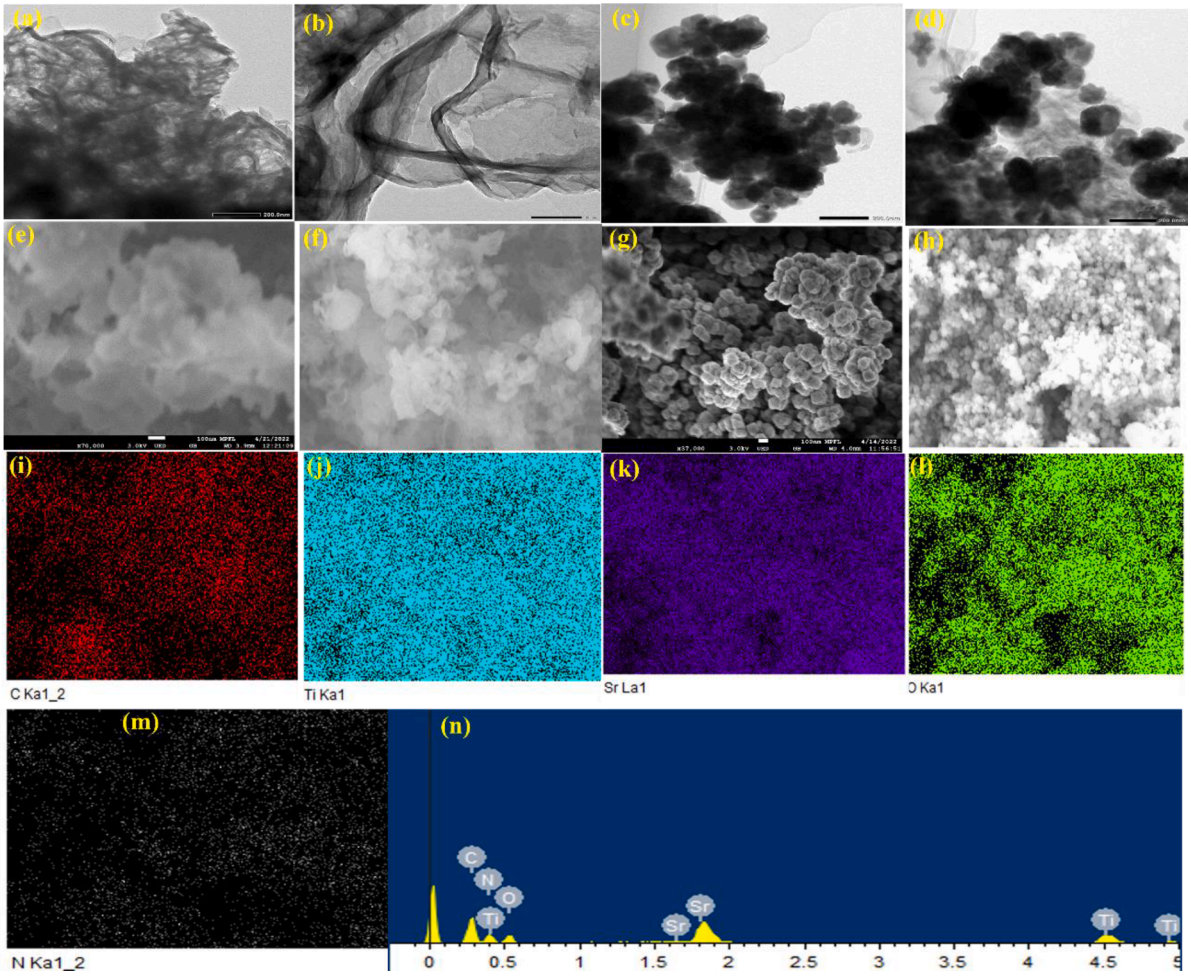

Fig. 3. Transmission electron microscope (TEM) pictures of **(a)** CN, **(b)** CN-$TAL_{10.0}$, **(c)** $SrTiO_3$ and **(d)** $SrTiO_3$/CN-$TAL_{10.0}$. Scanning electron microscopy (SEM) pictures of **(e)** CN, **(f)** CN-$TAL_{10.0}$ **(g)**, $SrTiO_3$, **(h)** $SrTiO_3$/CN-$TAL_{10.0}$ and **(i-m)** elemental mapping (**n**) and energy-dispersive X-ray spectroscopy (EDX) pictures of superior $SrTiO_3$/CN-$TAL_{10.0}$ catalyst.

composite, while that of negatively charged area in $SrTiO_3$/CN-$TAL_{10.0}$ might decrease the binding energy of Sr 3d, Ti 2p, and O 1s peaks. The obvious peaks can be seen in C 1s XPS spectra of CN at 300.1 & 302.3 eV for $SrTiO_3$/CN-$TAL_{10.0}$ and 286.1 & 284.6 eV, confirming the sp^2 hybridized carbon (C═N) and graphitic carbon (**Fig. 4 d, e**). Similarly, the N 1s spectrum for CN, showing four distinctive bands with binding energies at 406.2, 405.1, 406.9 and 409.1, indicated the sp^2 hybridized C-N═C bonds, tertiary nitrogen N-$(C)_3$, C—N—H groups, along with confined positive charges inside the heterojunction (Fig. 4**g**) [78,79]. The pyrrolic-N [N-$(C)_3$] and graphitic-N (CN-H) peaks, were shifted to the lower binding energies after combining with $SrTiO_3$ (Fig. 4**f**), which showed the flowing of electron from $SrTiO_3$ to triazine rings of CN between $SrTiO_3$/CN-$TAL_{10.0}$ composites interface (397.5 & 403.1 eV). The main peak in O 1s (Fig. 4**h**) was detected at 533.7 eV, which is due to the adsorption of oxygen species via chemisorption pathway over sample surface sites, whereas lattice oxygen O_2^- species peak (534.8) displays a positive change comparatively intricate from moistures of air during synthesis as well as for CN. The variation of all samples of XPS spectrum might be attributed to the electron transfer phenomenon from CN to $SrTiO_3$/CN-$TAL_{10.0}$ [80] (**Fig. S2**).

To investigate the electronic structure and activity enhancement of the prepared composites, we used Gaussian 09 computer software to perform density functional theory (DFT) calculations using the B3LYP/6-31G** functional theory [81-84 66 85]. The optimized structures of CN, CN-$TAL_{10.0}$ and $SrTiO_3$/CN-$TAL_{10.0}$ are illustrated in Fig. 5**a-e**, with the adsorption energy calculated by using Eq. (1).

$$\Delta E_{ads} = E(SrTiO_3/CN-TAL) - E(CN) - E(TAL) - E(SrTiO_3) \quad (1)$$

where E($SrTiO_3$/CN-TAL), E(CN), E(TAL) and E($SrTiO_3$) are the energies of $SrTiO_3$/CN-TAL, CN, TAL and $SrTiO_3$, respectively.

The basic equation formalism was used in concurrence through polarizable-continuum model in order to investigate the impact of solvent (water) over the interface amid TAL and $SrTiO_3$ molecules, those are found inside the CN based composite material. This investigation was carried out with the goal of better understanding the hybrid CN material. Calculations were done to determine the energies of maximum engaged molecule, the orbital (HOMO) orbital along with smallest untenanted molecular orbital (LUMO) for both CN and $SrTiO_3$/CN-$TAL_{10.0}$. This was done that the quantum-reactivity descriptors could be quantified to a greater degree. The $SrTiO_3$/CN-$TAL_{10.0}$ composite was proven as an extremely reactive sample by altering the diffusion of very stable nanoparticles of $SrTiO_3$, as shown by their lower HOMO-LUMO gap., which led to the conclusion that it possesses a high degree of reactivity (Fig. 5**c-e**) (Fig. 5**c-e**) [81,86,87]. In addition, the density of states (DOS) calculation was carried out for the CN material, as well as for the TAL-

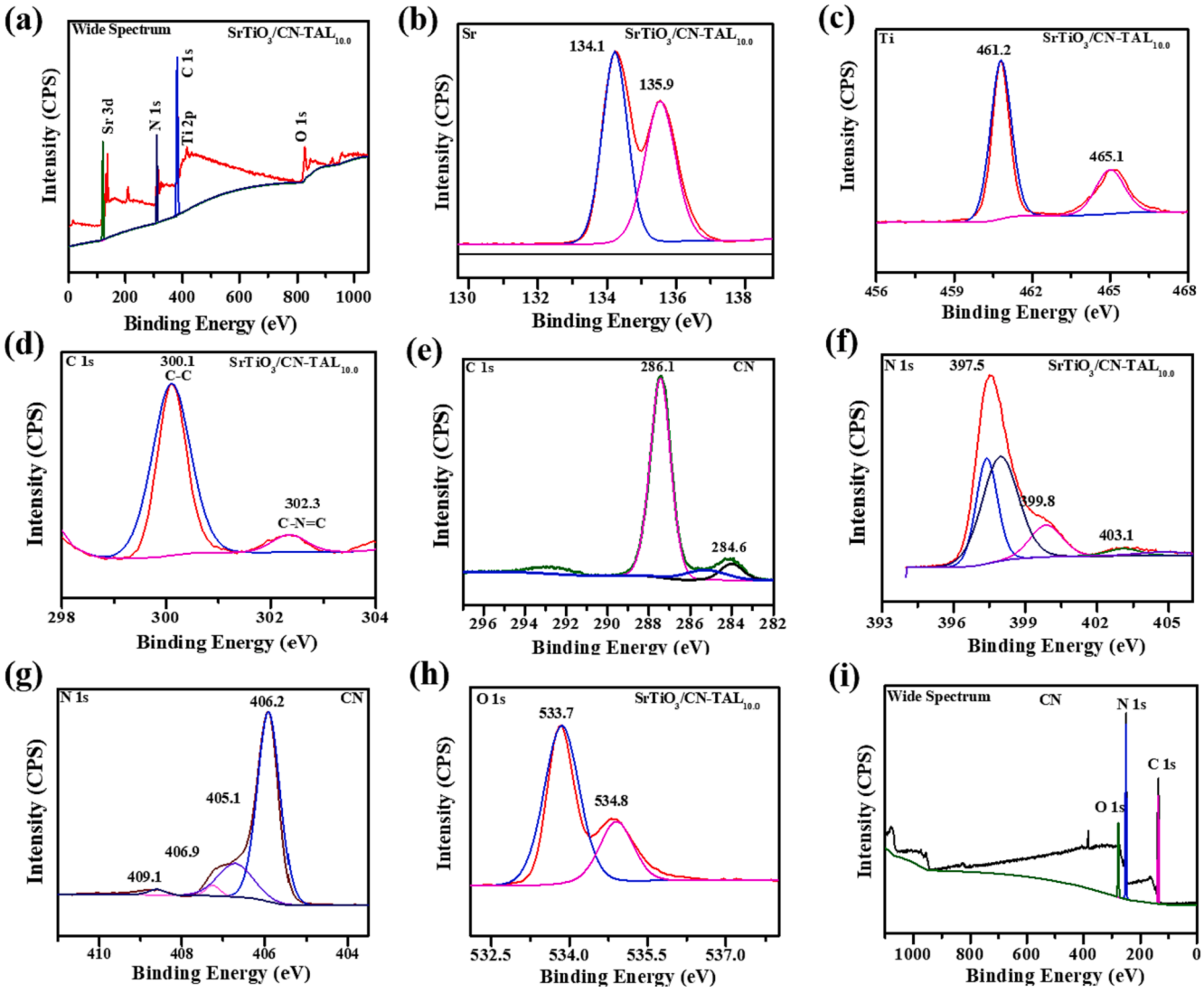

Fig. 4. X-ray photoelectron spectra (XPS). **(a)** Wide spectrum of $SrTiO_3$/CN-$TAL_{10.0}$., **(b)** high-resolution spectra of Sr of $SrTiO_3$/CN-$TAL_{10.0}$, **(c)** Ti, **(d)** C 1s, **(e)** C 1s of CN, **(f)** N 1s, of $SrTiO_3$/CN-$TAL_{10.0}$, **(g)** N 1s of CN, **(h)** O 1s of $SrTiO_3$/CN-$TAL_{10.0}$, and **(i)** CN spectrum of $SrTiO_3$/CN-$TAL_{10.0}$ material.

CN material and the $SrTiO_3$/CN-$TAL_{10.0}$ material, as can be seen in Fig. 5**f-g**. This was done to support the previously discussed concept. The results show that for the $SrTiO_3$/CN-TAL hybrid, C2p state govern both CB and the VB. Additionally, bandgap of 2.09 eV is displayed equally via both C2p and N2p states. The decrease in bandgap value demonstrates that the reactivity of $SrTiO_3$ with CN contributes to an increase in the material's photocatalytic activity (1.73 eV).

4. Photocatalytic hydrogen evolution

The photocatalytic hydrogen evolution reaction (HER) was carried out by using 50 mg of photocatalyst in 100 mL of deionized water by taking platinum (Pt) as a co-catalyst 3 wt% as well as triethanolamine (TEOA), as electron donor (sacrificial agents), in reaction reactor under visible light ($\lambda = 420$ nm). The reaction was performed at 12 °C using a circulated cooled system attached to the reaction system. The materials were critically assessed for 1 h in order to determine their anticipated photocatalytic activities. Under the identical condition, the pristine CN sample was used to determine its photocatalytic H_2 evolution, and a total efficiency of 15.6 umol/h^1 was observed. The CN-$TAL_{10.0}$ and CN-$TAL_{20.0}$ comparatively yielded higher HER efficiency of 193.6 and 146.5 umol/h^1, which clearly indicate the remarkable contribution of the integration of aromatic π-conjugated monomer, thiophenedicarboxaldehyde (TAL) within the matrix of CN. Owing to greater performance of CN-$TAL_{10.0}$, our superior outclass sample (CN-$TAL_{10.0}$) was combined with perovskite structure strontium-titanium ($SrTiO_3$), and the resultant heterojunction composite ($SrTiO_3$/CN-$TAL_{10.0}$) exhibited outstanding HER of 285.9 μmol/h^1, which is found to be eighteen times higher than that of pristine CN sample, **(**Fig. 6**a)**. Such a remarkable increase in the photocatalytic efficacy of a $SrTiO_3$/CN-$TAL_{10.0}$ might be attributed to the integration of co-monomer TAL and $SrTiO_3$ within the matrix of CN. This in turn enhances the overall light absorption intensity of heterojunction with a lessened charge recombination rate and an increase in surface area by showing ample surface-active sites for enhanced photocatalytic H_2 generation at the CB. For comparison, the $SrTiO_3$ was also combined with pristine CN and the obtained result reveals a rate of 102.5 umol/h^1 of HER, which was three times lower than photocatalytic HER yield of $SrTiO_3$/CN-$TAL_{10.0}$ but six times higher than that of pristine CN (Fig. 6**a**). Furthermore, recyclability of predominant samples (CN, CN-$TAL_{10.0}$ and $SrTiO_3$/CN-$TAL_{10.0}$) was assessed five times for 25 h (Fig. 6**b**). The results showed declines in HER even in the last phase, which might be due to co-erosion of the co-catalyst and the swift confession of additional chemicals over the interface of photocatalysts. Moreover, Fig. 6**c** showed the photocatalytic evolution of H_2 source by using all samples under the same conditions. Obtained finding indicates that the doping strategy and co-polymerization process could excellently increase the photocatalytic activity of CN during sun light illumination. In addition to that, several photocatalytic tests using CN, CN-$TAL_{10.0}$ and $SrTiO_3$/CN-$TAL_{10.0}$, were conducted to determine the potential impact of numerous irradiance levels. Hence, it becomes readily noticeable that apparent quantum yield (AQY), which is based on wavelength towards particular HER, is closely associated with relevant light intensity **(**Fig. 6**d)**. The activity of the CN sample towards HER was found to be consistently poor over the entire optical range until 550 nm, as compared to CN-$TAL_{10.0}$ and $SrTiO_3$/CN-$TAL_{10.0}$. In addition to considerable absorption capacity, the normal photocatalytic performance of CN-$TAL_{10.0}$ and $SrTiO_3$/CN-$TAL_{10.0}$, also showed a strong adsorption wavelength with good HER activity, respectively. Obtained findings indicate the considerable contribution of different regions of visible light (filter cut off). However, the CN-$TAL_{10.0}$ and $SrTiO_3$/CN-$TAL_{10.0}$ extend their photocatalytic optical range nearly to 550 nm and thus, liberate a highly energized performance for HER than that of CN **(**Fig. 6**d)**. The CB of the superior $SrTiO_3$/CN-$TAL_{10.0}$ sample towards HER is clearly explained in Fig. 6**e**, thus, revealing that the H_2 production source occurs in the CB region of photocatalyst owing to photoexcitation of electrons. Furthermore, some more tests were conducted to compare the enclosure of TEOA with other sacrificial agents such as lactic acid **(**Fig. 6**f)** under the identical conditions. According to the

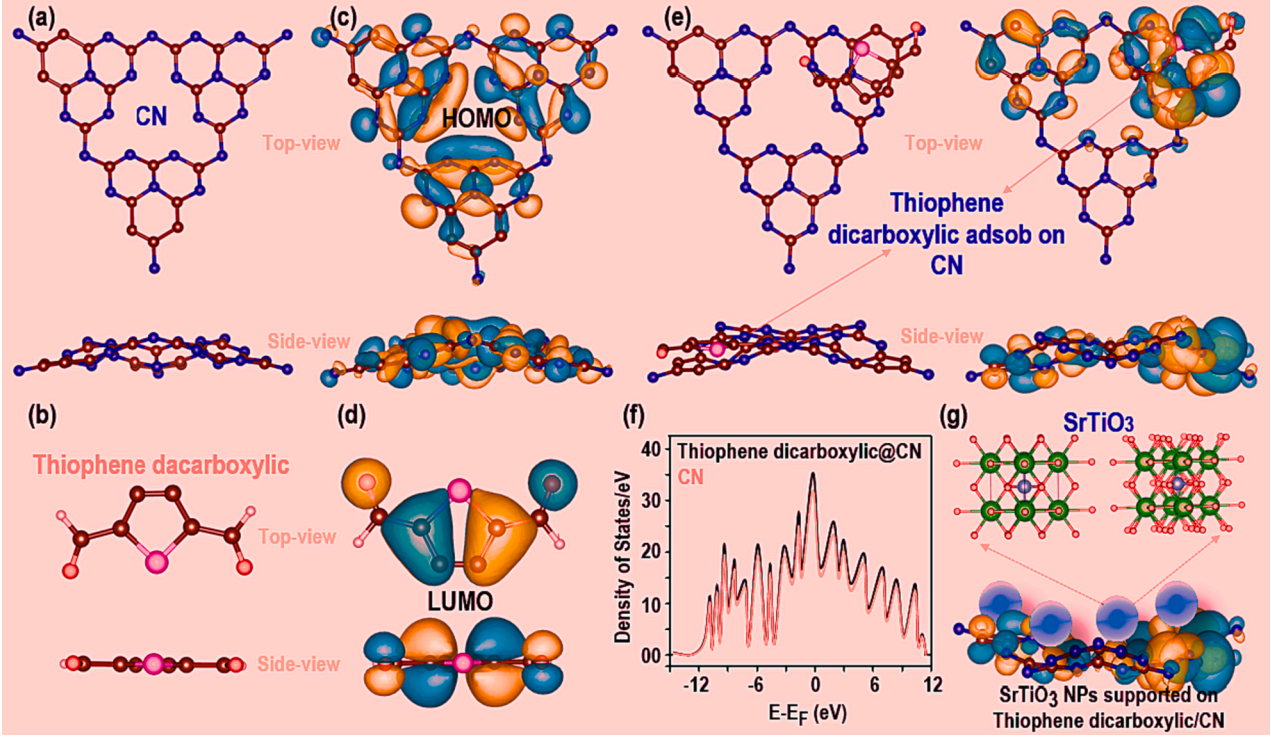

Fig. 5. The side and top-views of **(a)** optimized geometry of CN, **(b)** TAL, **(c)** HOMO of CN, **(d)** LUMO of TAL, **(e)** optimized geometry of CN-TAL and charge interaction between HOMO of CN and LUMO of TAL, **(f)** DOS of $SrTiO_3$/CN-$TAL_{10.0}$ material and **(g)** design of $SrTiO_3$/CN-$TAL_{10.0}$ architecture (Image holding via arrows shows basic unit cell of $SrTiO_3$).

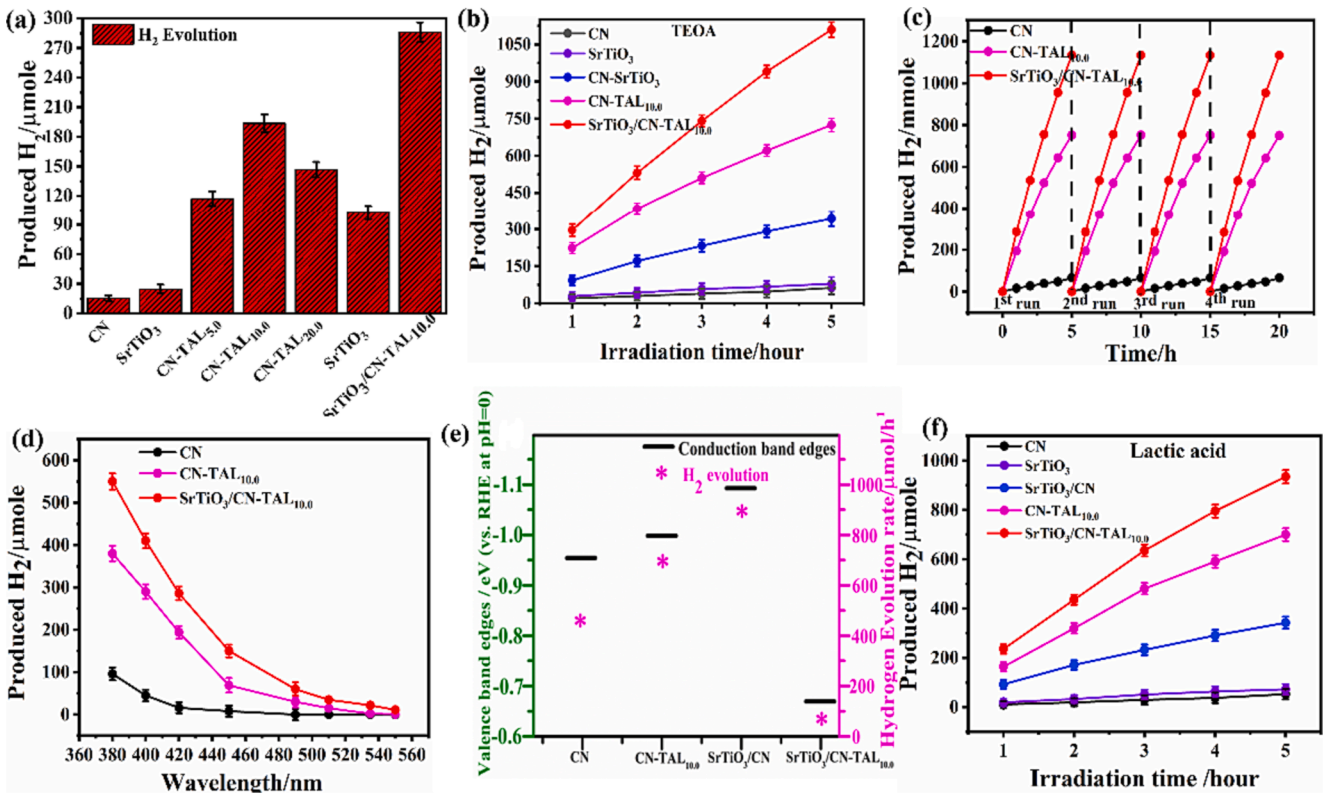

Fig. 6. Photocatalytic application of HER. **(a)** HER of optimized photocatalysts under similar conditions **(b)** Time-dependent production of H_2 among pristine and modified photocatalysts, **(c)** evaluation of the catalyst after different recycling experiment, **(d)** wavelength-based analyses, **(e)** CB of HER performance and **(f)** HER in the presence of lactic acid under solar light illumination (λ = 420 nm) with triplicates experiments error bars.

above-discussed results, the as-synthesized samples revealed enhanced photocatalytic performance for H_2 consumption under water splitting only with the aid of TEOA as a sacrificial agent (Fig. 6**f**). After long term stability test of photocatalysis, the superior sample i.e., $SrTiO_3$/CN-$TAL_{10.0}$ has been evaluated for various integral analysis such as XRD, XPS and morphology demonstrating some fluctuation as seen in **Fig. S1, S2 S3 & S4** (Supporting Information) respectively. The XRD pattern provides the similar diffraction peaks likewise the sample prior to use for photocatalytic water splitting. Moreover, the superior sample morphology indicates the hollow type structure of $SrTiO_3$/CN-$TAL_{10.0}$, which is might be due to the co-erosion of sample during water splitting process. The XPS survey spectrum shows the stability of sample with all original elements with no higher variation in their peaks. By following that, the time-resolved fluorescence decay spectra of both materials were also performed in order to measure the degree of exciton recombination. Three exponential functions could effectively fit their decay curves, and the average lives of $SrTiO_3$/CN-$TAL_{10.0}$ and CN were determined to be 5.25 ns and 1.05 ns, separately. The longer lifetime of $SrTiO_3$/CN-$TAL_{10.0}$, might be attributed to its fully -conjugated in-plane structure, which successfully enhance the charge separation by decreasing the charge recombination behaviour [88]. The raman spectroscopy was conducted to the confirm chemical structures of all photocatalyst **Fig. S5**. In CN, D peak and G peak in CN at (1239 cm^{-1} and 1521 cm^{-1}), indicates the disordered carbon in the CN along with its graphite form [89], which seems to be unclear in the CN-$TAL_{10.0}$. Moreover, the peaks appeared at 711, 901, 1239 cm^{-1} are allocated for the stretching vibration of aromatic C—N heterocycle properties of carbon and found to be weaker in CN-$TAL_{10.0}$. Collectively, the peaks between 700 and 1250 cm^{-1} are connected with various kinds of ring breathing modes of s-triazine [90,91]. According to earlier reports in undoped $SrTiO_3$, CN/$SrTiO_3$, $SrTiO_3$/CN-$TAL_{10.0}$, the broad bands appeared at around 250–500 and 600–800 cm^{-1} regions are related to the second-order raman scattering. The peaks at 143, 516 cm^{-1} well matched with TO_2, $TO_{4,\ frequencies}$, respectively, and revealing the first-order scattering actions [92]. The weak peak at 516 cm^{-1} belongs to the first-order raman scattering of TO_x phonon in $SrTiO_3$ too. Moreover, the weak vibration peaks at 143, 516, cm^{-1} could also be ascribed to A1 (TO) mode, along with showing the long-range lattice alteration in the cubic structure of $SrTiO_3$ [93].

5. Photocatalytic mechanism

Compared to those of other samples, the thiophenedicarboxaldehyde (TAL) and strontium-titanium ($SrTiO_3$) decorated carbon nitride (CN) heterojunction showed much increase in the photocatalytic activity towards hydrogen evolution, due to maximum visible light harvesting capacity of superior sample, as it produced too much electrons in the conduction band (CB) and holes in the valence band (VB) of sample as well as the formation of active species. The conjugated monomer TAL under visible light irradiation indicated a remarkable capacity to generate electrons in CB. Furthermore, the semi conductive $SrTiO_3$ sample plays a vital role to boost the transportation of electrons and the hole formation in a $SrTiO_3$/CN-$TAL_{10.0}$ heterojunction. The concept of photocatalysis phenomena is based on the sensitizer reagent, potential level, and double charge transfer mechanism. Although the CB position of CN is more negative than CB position of $SrTiO_3$, the photoinduced electrons will shift from CB of CN to $SrTiO_3$, making an offset of 0.89 eV. The enduring holes automatically moves from VB of $SrTiO_3$ to CN with

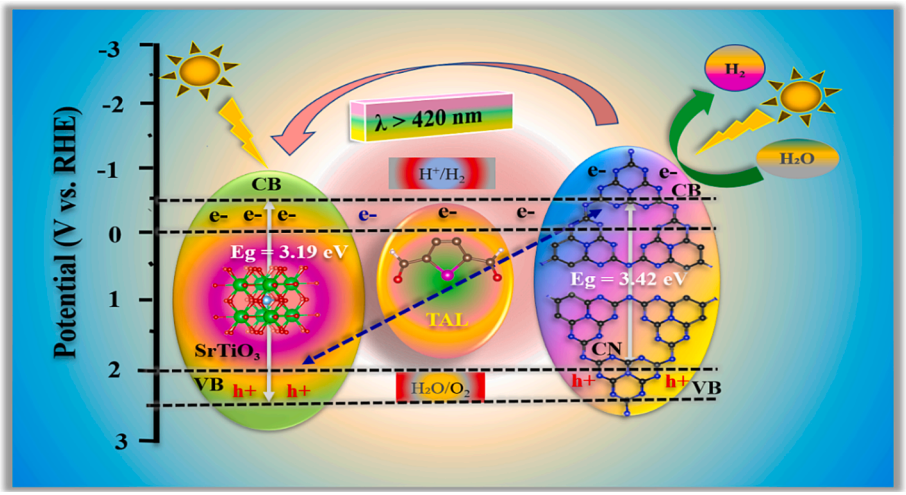

Fig. 7. The proposed mechanism for the photocatalytic hydrogen evolution using the $SrTiO_3$/CN-$TAL_{10.0}$ heterojunction process.

an offset of 0.06 eV. Therefore, the photoinduced electrons on the photocatalyst interface may quickly convert oxygen into superoxide ($^{\bullet}O_2^-$) radicals. In our view, both the experimental data and computational modelling now are fully consistent with our mechanism. According to Fig. 7**,** the CB and VB adjustments of $SrTiO_3$/CN-$TAL_{10.0}$ heterojunction are in better location respectively. After the energization of electron, they quickly transfer to the CB of photocatalyst, which is responsible for the photoreduction process (HER) of water. The role of CN, $SrTiO_3$ and the heterojunction $SrTiO_3$/CN-TAL10.0 as well as how electrons are moving from CB of CN to CB of $SrTiO_3$ is presented in Fig. 7, where organic conjugated TAL monomer acts as a mediator and boost the transportation of electron from CN to $SrTiO_3$. During whole process, the accumulated electron at the CB of $SrTiO_3$ further transfers to VB of CN and then excited towards CB of CN followed by CB of $SrTiO_3$ to make an efficient transportation channel of electrons between two semiconductors due to TAL under visible illumination in Fig. 7**.**

6. Conclusions

In conclusion, the $SrTiO_3$/CN-$TAL_{10.0}$ based photocatalyst was prepared via facile two step procedure of $SrTiO_3$ impregnation in order to produce the effect of a novel previously unexplored organic ligand thiophenedicarboxaldehyde incorporated CN. The as-obtained photocatalyst was further used in photocatalytic water splitting reaction for H_2 production under visible light. The results clearly show a considerable potential of a novel $SrTiO_3$/CN-$TAL_{10.0}$, with an outstanding H_2 production rate up to 285 μmol/h^1 at 283 K, those are found to be superior than the results reported in literature by using simple transition metals and CN based photocatalyst [70,94]. On the one hand, this outstanding photocatalytic activity is due to increased electron via $SrTiO_3$ nanoparticles, and rapidly combine with H^+ in the solution for high-capacity generation of H_2 energy. On the other hand, it can be attributed to a decrease in band gap from 3.42 to 2.66 eV, owing to the integration of $SrTiO_3$ and TAL monomer in the CN structure. The reciprocated impact of three compounds in the form of $SrTiO_3$/CN-$TAL_{10.0}$ brings up a substantial decrease in the recombination of photogenerated electron-hole, thus enhancing the overall production rate of H_2. Accordingly, the presented work provides novel insights and highlights the potential of their synergistic effects on charge steering for boosting photocatalysis in the form of sustainable energy conversion and production.

CRediT authorship contribution statement

Zeeshan Ajmal: Conceptualization, Formal analysis, Investigation, Data curation, Validation, Writing – original draft, Writing – review & editing. **Mahmood Ul Haq:** Conceptualization, Formal analysis, Investigation, Data curation. **Shahid Zaman:** Formal analysis, Investigation, Writing – original draft. **M.K. Al-Muhanna:** Investigation, Visualization, Writing – original draft. **Anuj Kumar:** Software, Visualization, Investigation. **Mohammed M. Fadhali:** Software, Visualization, Investigation. **Siwar Ben Hadj Hassine:** Investigation, Project administration. **Muhammad Qasim:** Investigation, Visualization. **K.F. Alshammari:** Software. **Ghulam Abbas Ashraf:** Visualization, Investigation, Supervision. **Abdul Qadeer:** Investigation, Software, Visualization. **Adil Murtaza:** Resources, Supervision, Writing – original draft, Project administration. **Sulaiman Al-Sulaimi:** Investigation, Methodology. **Huaqiang Zeng:** Conceptualization, Supervision, Writing – review & editing.

Declaration of Competing Interest

The authors declare that they have no known competing financial interests or personal relationships that could have appeared to influence the work reported in this paper.

Data availability

Data will be made available on request.

Acknowledgment

The authors extend their appreciation to the Deanship of Scientific Research at King Khalid University for funding this work through large group Research Project under grant number RGP2/80/44.

Appendix A. Supplementary data

Supplementary data to this article can be found online at https://doi.org/10.1016/j.jcis.2023.10.020.

References

[1] H. Ali, S. Ahmed, A. Hsini, S. Kizito, Y. Naciri, R. Djellabi, M. Abid, W. Raza, N. Hassan, M. Saif Ur Rehman, A. Jamal Khan, M. Khan, M. Zia Ul Haq, D. Aboagye, M. Kashif Irshad, M. Hassan, A. Hayat, B. Wu, A. Qadeer, Z. Ajmal, Efficiency of a novel nitrogen-doped Fe_3O_4 impregnated biochar (N/Fe_3O_4@BC) for arsenic (III and V) removal from aqueous solution: Insight into mechanistic understanding and reusability potential, Arabian J. Chem. 15 (11) (2022), 104209.

[2] A. Hayat, M. Sohail, A. El Jery, K.M. Al-Zaydi, K.F. Alshammari, J. Khan, H. Ali, Z. Ajmal, T.A. Taha, I. Ud Din, R. Altamimi, M.A. Hussein, Y. Al-Hadeethi, Y. Orooji, M.Z. Ansari, Different Dimensionalities, Morphological Advancements and Engineering of g-C_3N_4-Based Nanomaterials for Energy Conversion and Storage, Chem. Rec. 23 (5) (2023) e202200171.

[3] A. Malik, M. Hussain, F. Uddin, W. Raza, S. Hussain, U.-e.- Habiba, T. Malik, Z. Ajmal, Investigation of textile dyeing effluent using activated sludge system to assess the removal efficiency, Water. Environ. Res 93 (12) (2021) 2931–2940.

[4] Z. Ajmal, M. Usman, I. Anastopoulos, A. Qadeer, R. Zhu, A. Wakeel, R. Dong, Use of nano-/micro-magnetite for abatement of cadmium and lead contamination, J. Environ. Manage 264 (2020), 110477.

[5] D. Zeng, T. Zhou, W.-J. Ong, M. Wu, X. Duan, W. Xu, Y. Chen, Y.-A. Zhu, D.-L. Peng, Sub-5 nm Ultra-Fine FeP Nanodots as Efficient Co-Catalysts Modified Porous g-C_3N_4 for Precious-Metal-Free Photocatalytic Hydrogen Evolution under Visible Light, ACS Appl. Mater. Interfaces 11 (6) (2019) 5651–5660.

[6] A. Hayat, M. Sohail, A.E. Jery, K.M. Al-Zaydi, S. Raza, H. Ali, Z. Ajmal, A. Zada, T. A. Taha, I.U. Din, M.A. Khan, M.A. Amin, Y. Al-Hadeethi, A.Z. Barasheed, Y. Orooji, J. Khan, M.Z. Ansari, Recent advances, properties, fabrication and opportunities in two-dimensional materials for their potential sustainable applications, Energy Storage Mater. 59 (2023), 102780.

[7] Z. Ajmal, T.A. Taha, M.A. Amin, A. Palamanit, W.I. Nawawi, A. Kalam, A.G. Al-Sehemi, H. Algarni, A. Qadeer, H. Ali, A. Kumar, J. Qian, A. Hayat, H. Zeng, Embedding Aromatic Conjugated Monomer within Carbon Nitride for Efficient Photocatalytic Reduction Reactions, J. Mol. Liq. 368 (2022), 120617.

[8] X. Wang, Q. Li, L. Gan, X. Ji, F. Chen, X. Peng, R. Zhang, 3D macropore carbon-vacancy g-C_3N_4 constructed using polymethylmethacrylate spheres for enhanced photocatalytic H_2 evolution and CO_2 reduction, J. Energy. Chem. 53 (2021) 139–146.

[9] A. Hayat, M. Sohail, T.A. Taha, S. Kumar Baburao Mane, A.G. Al-Sehemi, A.A. Al-Ghamdi, W.I. Nawawi, A. Palamanit, M.A. Amin, A.M. Fallatah, Z. Ajmal, H. Ali, W. Ullah Khan, M. Wajid Shah, J. Khan, S. Wageh, Synergetic effect of bismuth vanadate over copolymerized carbon nitride composites for highly efficient photocatalytic H_2 and O_2 generation, J. Colloid Interface Sci. 627 (2022) 621–629.

[10] A. Hayat, J.A. Shah Syed, A.G. Al-Sehemi, K.S. El-Nasser, T.A. Taha, A.A. Al-Ghamdi, M.A. Amin, Z. Ajmal, W. Iqbal, A. Palamanit, D.I. Medina, W.I. Nawawi, M. Sohail, State of the art advancement in rational design of g-C_3N_4 photocatalyst for efficient solar fuel transformation, environmental decontamination and future perspectives, Int. J. Hydrogen Energy 47 (20) (2022) 10837–10867.

[11] G. Bharath, G. Karthikeyan, A. Kumar, J. Prakash, D. Venkatasubbu, A. Kumar Nadda, V. Kumar Gupta, M. Abu Haija, F. Banat, Surface engineering of Au nanostructures for plasmon-enhanced electrochemical reduction of N_2 and CO_2 into urea in the visible-NIR region, Appl. Energy 318 (2022), 119244.

[12] Z. Ajmal, Y. Naciri, A. Hsini, B.M. Bresolin, A. Qadeer, M. Nauman, M. Arif, M. K. Irshad, K.A. Khan, R. Djellabi, C.L. Bianchi, M. Laabd, A. Albourine, R. Dong, Prospects of Photocatalysis in the Management of Nitrate Contamination in Potable Water, in: N.A. Oladoja, E.I. Unuabonah (Eds.), Progress and Prospects in the Management of Oxyanion Polluted Aqua Systems, Springer International Publishing, Cham, 2021, pp. 185–217.

[13] S. Zaman, A.I. Douka, L. Noureen, X. Tian, Z. Ajmal, H. Wang, Oxygen reduction performance measurements: Discrepancies against benchmarks, Battery Energy 2 (3) (2023) 20220060.

[14] A. Hayat, M. Sohail, A. El Jery, K.M. Al-Zaydi, S. Raza, H. Ali, Y. Al-Hadeethi, T. A. Taha, I. Ud Din, M. Ali Khan, M.A. Amin, E. Ghasali, Y. Orooji, Z. Ajmal, M. Zahid Ansari, Recent advances in ground-breaking conjugated microporous polymers-based materials, their synthesis, modification and potential applications, Mater. Today 64 (2023) 180–208.

[15] Z. Ajmal, A. Qadeer, U. Khan, M. Bilal Hussain, M. Irfan, R. Mehmood, M. Abid, R. Djellabi, A. Kumar, H. Ali, A. Kalam, A.G. Al-Sehemi, H. Algarni, Y. Al-Hadeethi, J. Qian, A. Hayat, H. Zeng, Current progresses in two-dimensional MXene-based framework: prospects from superficial synthesis to energy conversion and storage applications, Mater. Today Chem. 27 (2023), 101238.

[16] Z. Ajmal, Y. Naciri, M. Ahmad, A. Hsini, A. Bouziani, M. Laabd, W. Raza, A. Murtaza, A. Kumar, S. Ullah, A.G. Al-Sehemi, A.A. Al-Ghamdi, A. Qadeer, A. Hayat, R. Djellabi, Use of conductive polymer-supported oxide-based photocatalysts for efficient VOCs & SVOCs removal in gas/liquid phase, J. Environ. Chem. Eng. 11 (1) (2023), 108935.

[17] Z. Ajmal, A. Muhmood, M. Usman, S. Kizito, J. Lu, R. Dong, S. Wu, Phosphate removal from aqueous solution using iron oxides: Adsorption, desorption and regeneration characteristics, J. Colloid. Interf. Sci 528 (2018) 145–155.

[18] A. Qadeer, K.L. Kirsten, Z. Ajmal, Z. Xingru, Rebuttal to Comment on "Alternative Plasticizers As Emerging Global Environmental and Health Threat: Another Regrettable Substitution?" Focus on DINCH as an Example, Environ. Sci. Technol. 56 (8) (2022) 5294–5297.

[19] M.R. Hoffmann, S.T. Martin, W. Choi, D.W. Bahnemann, Environmental Applications of Semiconductor Photocatalysis, Chem. Rev 95 (1) (1995) 69–96.

[20] S. Kizito, H. Luo, S. Wu, Z. Ajmal, T. Lv, R. Dong, Phosphate recovery from liquid fraction of anaerobic digestate using four slow pyrolyzed biochars: Dynamics of adsorption, desorption and regeneration, J. Environ. Manage. 201 (2017) 260–267.

[21] Z. Ajmal, A. Muhmood, R. Dong, S. Wu, Probing the efficiency of magnetically modified biomass-derived biochar for effective phosphate removal, J. Environ. Manage 253 (2020), 109730.

[22] Z. Ajmal, M.U. Haq, Y. Naciri, R. Djellabi, N. Hassan, S. Zaman, A. Murtaza, A. Kumar, A.G. Al-Sehemi, H. Algarni, O.A. Al-Hartomy, R. Dong, A. Hayat, A. Qadeer, Recent advancement in conjugated polymers based photocatalytic technology for air pollutants abatement: Cases of CO_2, NO_x, and VOCs, Chemosphere 308 (2022), 136358.

[23] Y. Naciri, A. Hsini, Z. Ajmal, A. Bouddouch, B. Bakiz, J.A. Navío, A. Albourine, J. C. Valmalette, M. Ezahri, A. Benlhachemi, Influence of Sr-doping on structural, optical and photocatalytic properties of synthesized $Ca_3(PO_4)_2$, J. Colloid. Interf. Sci. 572 (2020) 269–280.

[24] J. Yi, W. El-Alami, Y. Song, H. Li, P.M. Ajayan, H. Xu, Emerging surface strategies on graphitic carbon nitride for solar driven water splitting, Chem. Eng. J. 382 (2020), 122812.

[25] A. Hayat, M. Sohail, U. Anwar, T.A. Taha, K.S. El-Nasser, A.M. Alenad, A.G. Al-Sehemi, N. Ahmad Alghamdi, O.A. Al-Hartomy, M.A. Amin, A. Alhadhrami, A. Palamanit, S.K.B. Mane, W.I. Nawawi, Z. Ajmal, Enhanced photocatalytic overall water splitting from an assembly of donor-π-acceptor conjugated polymeric carbon nitride, J. Colloid. Interf. Sci. 624 (2022) 411–422.

[26] Z. Ajmal, A. Hayat, M. Qasim, A. Kumar, A. El Jery, W. Abbas, M.B. Hussain, A. Qadeer, S. Iqbal, S. Bashir, Z. Ahmad, J. Qian, A. Murtaza, H. Zeng, Assembly of a novel Fe_2TiO_5-impregnated donor-π-acceptor conjugated carbon nitride for highly efficient solar water splitting, Sustain. Mater. Technol. 36 (2023) e00594.

[27] S. Khan, Z. Ajmal, S. Mahmood, M. ul Haq, Synthesis of mesoporous composites based on α-Fe_2O_3/NiO nanowires for the photocatalytic degradation of rhodamine B dye, New J. Chem. 47 (21) (2023) 10333–10346.

[28] Y. Naciri, A. Hsini, Z. Ajmal, J.A. Navío, B. Bakiz, A. Albourine, M. Ezahri, A. Benlhachemi, Recent progress on the enhancement of photocatalytic properties of $BiPO_4$ using π–conjugated materials, Adv. Colloid Interface Sci. 280 (2020), 102160.

[29] L. Liu, P.Y. Yu, X. Chen, S.S. Mao, D.Z. Shen, Hydrogenation and Disorder in Engineered Black TiO_2, Phy. Rev. Lett 111 (6) (2013), 065505.

[30] Q. Muhammad, X. Fei, L. Maochang, G. Liejin, Phase-transition-induced one-dimensional amorphous αFe_2O_3/β-FeOOH homojunction for efficient photocatalytic water oxidation, J. Photonics Energy 9 (2) (2019) 1–14.

[31] K. Sivula, Metal Oxide Photoelectrodes for Solar Fuel Production, Surface Traps, and Catalysis, J. Phy. Chem. Lett. 4 (10) (2013) 1624–1633.

[32] T.W. Hamann, Splitting water with rust: hematite photoelectrochemistry, Dalton. Trans. 41 (26) (2012) 7830–7834.

[33] Y. Wang, R. Godin, J.R. Durrant, J. Tang, Efficient Hole Trapping in Carbon Dot/Oxygen-Modified Carbon Nitride Heterojunction Photocatalysts for Enhanced Methanol Production from CO_2 under Neutral Conditions, Angew. Chem. Int. Ed. Engl. 60 (38) (2021) 20811–20816.

[34] I. Akihide, S. Kenji, K. Akihiko, Sensitization of $NaMO_3$ (M: Nb and Ta) Photocatalysts with Wide Band Gaps to Visible Light by Ir Doping, Bull. Chem. Soc. Jpn. 82 (4) (2009) 514–518.

[35] Y. Shimodaira, H. Kato, H. Kobayashi, A. Kudo, Investigations of Electronic Structures and Photocatalytic Activities under Visible Light Irradiation of Lead Molybdate Replaced with Chromium(VI), Bull. Chem. Soc. Jpn. 80 (5) (2007) 885–893.

[36] J. Kegel, I.M. Povey, M.E. Pemble, Zinc oxide for solar water splitting: A brief review of the material's challenges and associated opportunities, Nano Energy 54 (2018) 409–428.

[37] D. Jiang, Z. Sun, H. Jia, D. Lu, P. Du, A cocatalyst-free CdS nanorod/ZnS nanoparticle composite for high-performance visible-light-driven hydrogen production from water, J. Mater. Chem. A 4 (2) (2016) 675–683.

[38] A. Miyoshi, S. Nishioka, K. Maeda, Water Splitting on Rutile TiO_2 -Based Photocatalysts, Chemistry (Weinheim an der Bergstrasse, Germany) 24 (69) (2018) 18204–18219.

[39] H. Eidsvåg, S. Bentouba, P. Vajeeston, S. Yohi, D. Velauthapillai, TiO_2 as a Photocatalyst for Water Splitting-An Experimental and Theoretical Review, Molecules 26 (6) (2021).

[40] Y. Ham, T. Hisatomi, Y. Goto, Y. Moriya, Y. Sakata, A. Yamakata, J. Kubota, K. Domen, Flux-mediated doping of $SrTiO_3$ photocatalysts for efficient overall water splitting, J. Mater. Chem. A 4 (8) (2016) 3027–3033.

[41] W.-J. Ong, L.-L. Tan, Y.H. Ng, S.-T. Yong, S.-P. Chai, Graphitic Carbon Nitride (g-C_3N_4)-Based Photocatalysts for Artificial Photosynthesis and Environmental Remediation: Are We a Step Closer To Achieving Sustainability? Chem. Rev. 116 (12) (2016) 7159–7329.

[42] A. Hayat, M. Sohail, A. Qadeer, T.A. Taha, M. Hussain, S. Ullah, A.G. Al-Sehemi, H. Algarni, M.A. Amin, M. Aqeel Sarwar, W.I. Nawawi, A. Palamanit, Y. Orooji, Z. Ajmal, Recent Advancement in Rational Design Modulation of MXene: A Voyage from Environmental Remediation to Energy Conversion and Storage, Chem. Rec. 22 (12) (2022) e202200097.

[43] A. Hayat, M. Sohail, W. Iqbal, T.A. Taha, A.M. Alenad, A.G. Al-Sehemi, S. Ullah, N. A. Alghamdi, A. Alhadhrami, Z. Ajmal, A. Palamanit, W.I. Nawawi, H.S. AlSalem, H. Ali, A. Zada, M.A. Amin, Molecular engineering optimized carbon nitride photocatalyst for CO2 reduction to solar fuels, J. Sci.: Adv. Mater. Devices 7 (4) (2022), 100483.

[44] W. Li, M. Sohail, U. Anwar, T.A. Taha, A.G. Al-Sehemi, S. Muhammad, A.A. Al-Ghamdi, M.A. Amin, A. Palamanit, S. Ullah, A. Hayat, Z. Ajmal, Recent progress in g–C_3N_4–Based materials for remarkable photocatalytic sustainable energy, Int. J. Hydrogen Energy 47 (49) (2022) 21067–21118.

[45] Q. Lin, S. Liang, J. Wang, R. Zhang, G. Liu, X. Wang, Hierarchically Periodic Macroporous CdS–ZnO Heterojunctions with Multiple Quantum Well-like Band Alignments for Efficient Photocatalytic Hydrogen Evolution without a Cocatalyst, ACS Sustain. Chem. Eng. 11 (7) (2023) 3093–3102.

[46] X. Wang, Q. Li, Q. Lin, R. Zhang, M. Ding, CdS-sensitized 3D ordered macroporous g-C_3N_4 for enhanced visible-light photocatalytic hydrogen generation, J. Mater. Sci. Technol. 111 (2022) 204–210.

[47] P. Niu, L. Zhang, G. Liu, H.-M. Cheng, Graphene-Like Carbon Nitride Nanosheets for Improved Photocatalytic Activities, Adv. Funct. Mater. 22 (22) (2012) 4763–4770.

[48] X. Wang, K. Maeda, A. Thomas, K. Takanabe, G. Xin, J.M. Carlsson, K. Domen, M. Antonietti, A metal-free polymeric photocatalyst for hydrogen production from water under visible light, Nat. Mater. 8 (1) (2009) 76–80.

[49] A. Hayat, M. Sohail, U. Anwar, T.A. Taha, H.I.A. Qazi, Z. Amina, A.G. Ajmal, H. Al-Sehemi, A.A. Algarni, M.A. Al-Ghamdi, A. Amin, W.I. Palamanit, E.F. Nawawi, Y. O. Newair, A Targeted Review of Current Progress, Challenges and Future Perspective of g-C_3N_4 based Hybrid Photocatalyst Toward Multidimensional Applications, Chem. Rec. 23 (1) (2023) e202200143.

[50] X. Huo, Y. Yang, Q. Niu, Y. Zhu, G. Zeng, C. Lai, H. Yi, M. Li, Z. An, D. Huang, Y. Fu, B. Li, L. Li, M. Zhang, A direct Z-scheme oxygen vacant BWO/oxygen-enriched graphitic carbon nitride polymer heterojunction with enhanced photocatalytic activity, Chem. Eng. J. 403 (2021), 126363.

[51] Y. Huo, J. Zhang, Z. Wang, K. Dai, C. Pan, C. Liang, Efficient interfacial charge transfer of 2D/2D porous carbon nitride/bismuth oxychloride step-scheme heterojunction for boosted solar-driven CO_2 reduction, J. Colloid Interf. Sci. 585 (2021) 684–693.

[52] S. Ahmed, H.U. Rehman, Z. Ali, A. Qadeer, A. Haseeb, Z. Ajmal, Solvent assisted synthesis of hierarchical magnesium oxide flowers for adsorption of phosphate and methyl orange: Kinetic, isotherm, thermodynamic and removal mechanism, Surf. Interf. 23 (2021), 100953.

[53] M. Sohail, U. Anwar, T.A. Taha, H.I.A. Qazi, A.G. Al-Sehemi, S. Ullah, H. Algarni, I. M. Ahmed, M.A. Amin, A. Palamanit, W. Iqbal, S. Alharthi, W.I. Nawawi, Z. Ajmal, H. Ali, A. Hayat, Nanostructured materials based on g-C_3N_4 for enhanced photocatalytic activity and potentials application: A review, Arabian J. Chem. 15 (9) (2022), 104070.

[54] F. Pan, M. Sohail, T.A. Taha, A.G. Al-Sehemi, S. Ullah, H.S. AlSalem, G.A. M. Mersal, M.M. Ibrahim, A.M. Alenad, O.A. Al-Hartomy, M.A. Amin, Z. Ajmal, A. Palamanit, A. Hayat, A. Zada, W.I. Nawawi, A facile molecular aggregation of isoquinoline based g-C_3N_4 for high photocatalytic performance under visible light illumination, Mater. Res. Bull. 152 (2022), 111865.

[55] Y. Xu, M.A.A. Schoonen, The absolute energy positions of conduction and valence bands of selected semiconducting minerals, J American Mineralogist, Am. Mineral. 85 (3–4) (2000) 543–556.

[56] K. Iizuka, T. Wato, Y. Miseki, K. Saito, A. Kudo, Photocatalytic reduction of carbon dioxide over Ag cocatalyst-loaded $ALa_4Ti_4O_{15}$ (A = Ca, Sr, and Ba) using water as a reducing reagent, J. Am. Chem. Soc. 133 (51) (2011) 20863–20868.

[57] Z. Jiang, T. Xiao, V.L. Kuznetsov, P.P. Edwards, Turning carbon dioxide into fuel, Philos. Trans. A. Math. Phys Eng. Sci. 368 (1923) (2010) 3343–3364.

[58] Y. Bi, S. Ouyang, N. Umezawa, J. Cao, J. Ye, Facet effect of single-crystalline Ag_3PO_4 sub-microcrystals on photocatalytic properties, J. Am. Chem. Soc. 133 (17) (2011) 6490–6492.

[59] C. Zhao, C. Xiong, X. Liu, M. Qiao, Z. Li, T. Yuan, J. Wang, Y. Qu, X. Wang, F. Zhou, Q. Xu, S. Wang, M. Chen, W. Wang, Y. Li, T. Yao, Y. Wu, Y. Li, Unraveling the enzyme-like activity of heterogeneous single atom catalyst, Chem. Commun. 55 (16) (2019) 2285–2288.

[60] S. Yin, H. Yamaki, M. Komatsu, Q. Zhang, J. Wang, Q. Tang, F. Saito, T. Sato, Preparation of nitrogen-doped titania with high visible light induced photocatalytic activity by mechanochemical reaction of titania and hexamethylenetetramine, J. Mater. Chem 13 (12) (2003) 2996–3001.

[61] S. Kumar, T. Surendar, A. Baruah, V. Shanker, Synthesis of a novel and stable g-C_3N_4–Ag_3PO_4 hybrid nanocomposite photocatalyst and study of the photocatalytic activity under visible light irradiation, J. Mater. Chem. A 1 (17) (2013) 5333–5340.

[62] Y. Naciri, A. Hsini, A. Ahdour, B. Akhsassi, K. Fritah, Z. Ajmal, R. Djellabi, A. Bouziani, A. Taoufyq, B. Bakiz, A. Benlhachemi, M. Sillanpää, H. Li, Recent advances of bismuth titanate based photocatalysts engineering for enhanced organic contaminates oxidation in water: A review, Chemosphere 300 (2022), 134622.

[63] Y. Wang, Q. Wang, X. Zhan, F. Wang, M. Safdar, J. He, Visible light driven type II heterostructures and their enhanced photocatalysis properties: a review, Nanoscale 5 (18) (2013) 8326–8339.

[64] S. Kumar, S. Tonda, A. Baruah, B. Kumar, V. Shanker, Synthesis of novel and stable g-C_3N_4/N-doped $SrTiO_3$ hybrid nanocomposites with improved photocurrent and photocatalytic activity under visible light irradiation, Dalton Trans. 43 (42) (2014) 16105–16114.

[65] T.N.Q. Trang, M. Tran Van, T.B. Phan, V.T.H. Thu, Spatially Controlled Photogenerated Charge Carriers Induced by $SrTiO_3$-Architectured Heterojunction Nanocubes for a Photocatalytic Hydrogen Evolution Reaction, ACS Appl. Energy Mater. 4 (9) (2021) 8910–8921.

[66] G.T. M. Frisch, H. Schlegel, G. Scuseria, M. Robb, J. Cheeseman, G. Scalmani, V. Barone, G. Petersson, H. Nakatsuji, Gaussian 16, Revision A. 03, Gaussian,, Inc. Wallingford CT, 2016.

[67] S. Bahmanyar, K.N. Houk, H.J. Martin, B. List, Quantum mechanical predictions of the stereoselectivities of proline-catalyzed asymmetric intermolecular aldol reactions, J. Am. Chem. Soc. 125 (9) (2003) 2475–2479.

[68] M.K. Guediri, D. Chebli, A. Bouguettoucha, R. Bourzami, A. Amrane, Novel Fe_2TiO_5/reduced graphene oxide heterojunction photocatalyst with improved adsorption capacity and visible light photoactivity: experimental and DFT approach, Environ. Sci. Pollut. Res. 28 (7) (2021) 8507–8519.

[69] N. Kerru, L. Gummidi, S.V.H.S. Bhaskaruni, S.N. Maddila, P. Singh, S. B. Jonnalagadda, A comparison between observed and DFT calculations on structure of 5-(4-chlorophenyl)-2-amino-1,3,4-thiadiazole, Sci. Rep. 9 (1) (2019) 19280.

[70] X. Xu, G. Liu, C. Randorn, J.T.S. Irvine, g-C_3N_4 coated $SrTiO_3$ as an efficient photocatalyst for H_2 production in aqueous solution under visible light irradiation, Int. J. Hydrogen Energy 36 (21) (2011) 13501–13507.

[71] G. Yang, W. Yan, J. Wang, Q. Zhang, H. Yang, Fabrication and photocatalytic activities of $SrTiO_3$ nanofibers by sol–gel assisted electrospinning, J. Sol-Gel. Sci. Technol. 71 (1) (2014) 159–167.

[72] S.M. Alshehri, A. Aldalbahi, A.B. Al-hajji, A.A. Chaudhary, M.i.h. Panhuis, N. Alhokbany, T. Ahamad, Development of carboxymethyl cellulose-based hydrogel and nanosilver composite as antimicrobial agents for UTI pathogens, Carbohydr. Polym. 138 (2016) 229–236.

[73] N. Khalaf, T. Ahamad, M. Naushad, N. Al-hokbany, S.I. Al-Saeedi, S. Almotairi, S. M. Alshehri, Chitosan polymer complex derived nanocomposite (AgNPs/NSC) for electrochemical non-enzymatic glucose sensor, Int. J. Biol. Macromol. 146 (2020) 763–772.

[74] S. Sakthivel, M. Janczarek, H. Kisch, Visible Light Activity and Photoelectrochemical Properties of Nitrogen-Doped TiO_2, J. Phy. Chem. B 108 (50) (2004) 19384–19387.

[75] N. Shaishta, W.U. Khan, S. Mane, A. Hayat, G. Manjunatha, Redmitting $CaSc_2O_4$: Eu^{3+} phosphor for NUV-based warm white LEDs: structural elucidation and Hirshfeld surface analysis, Int. J. Energy Res. (2020).

[76] A. Ah, B. Ns, C. Iu, D. Mk, E. Skbmb, F. Ah, G. Iu, H. Aur, I. Ta, J. Gm, Molecular engineering of carbon nitride towards photocatalytic H_2 evolution and dye degradation, J. Colloid Interface Sci. (2021).

[77] A. Hayat, T.A. Taha, A.M. Alenad, I. Ullah, S. Shah, I. Uddin, I. Ullah, A. Hayat, W. U. Khan, A simplistic molecular agglomeration of carbon nitride for optimized photocatalytic performance, Surf. Interfaces (2021).

[78] X. Wei, C. Shao, X. Li, N. Lu, K. Wang, Z. Zhang, Y. Liu, Facile in situ synthesis of plasmonic nanoparticles-decorated g-C_3N_4/TiO_2 heterojunction nanofibers and comparison study of their photosynergistic effects for efficient photocatalytic H_2 evolution, Nanoscale 8 (21) (2016) 11034–11043.

[79] Z. Zhang, J. Huang, M. Zhang, Q. Yuan, B. Dong, Ultrathin hexagonal SnS_2 nanosheets coupled with g-C_3N_4 nanosheets as 2D/2D heterojunction photocatalysts toward high photocatalytic activity, Appl. Catal. B. 163 (2015) 298–305.

[80] T. Ahamad, S.M. Alshehri, Fabrication of Ag@$SrTiO_3$/g-C_3N_4 heterojunctions for H_2 production and the degradation of pesticides under visible light, Sep. Purif. Technol. 297 (2022), 121431.

[81] A. Kumar, G. Yasin, M. Tabish, D. Kumar Das, S. Ajmal, A. Kumar Nadda, G. Zhang, T. Maiyalagan, A. Saad, R.K. Gupta, M.M. Makhlouf, S. Ibraheem, A catalyst-free preparation of conjugated poly iron-phthalocyanine and its superior oxygen reduction reaction activity, Chem. Eng. J. 445 (2022), 136784.

[82] M. Tabish, J. Zhao, A. Kumar, J. Yan, J. Wang, F. Shi, J. Zhang, L. Peng, M. A. Mushtaq, G. Yasin, Developing Epoxy-based Anti-corrosion Functional Nanocomposite coating with CaFe-Tolyl-triazole Layered Double Hydroxide@g-C_3N_4 as Nanofillers on Q235 steel substrate against NaCl corrosive environment, Chem. Eng. J. 137624 (2022).

[83] J. Choi, T. Ingsel, D. Neupane, S.R. Mishra, A. Kumar, R.K. Gupta, Metal-organic framework-derived cobalt oxide and sulfide having nanoflowers architecture for efficient energy conversion and storage, J. Energy. Storage 50 (2022), 104145.

[84] K. Thompson, A. Kumar, D. Neupane, S.R. Mishra, F. Perez, R.K. Gupta, Synergistic Co–P bonding effect on hydrogen evolution reaction activity and supercapacitor applications of CoMoP material, Int. J. Hydro. Energy 47 (63) (2022) 26850–26858.

[85] K.A. Baseden, J.W. Tye, Introduction to Density Functional Theory: Calculations by Hand on the Helium Atom, J. Chem. Edu. 91 (12) (2014) 2116–2123.

[86] Z. Yang, Z. Mao, X. Zhang, D. Ou, Y. Mu, Y. Zhang, C. Zhao, S. Liu, Z. Chi, J. Xu, Y.-C. Wu, P.-Y. Lu, A. Lien, M.R. Bryce, Intermolecular Electronic Coupling of Organic

Units for Efficient Persistent Room-Temperature Phosphorescence, Angew. Chem. Int. Ed. 55 (6) (2016) 2181–2185.
[87] H. Bentour, M. Boujnah, M. Houmad, M. El Yadari, A. Benyoussef, A. El Kenz, DFT study of Se and Te doped $SrTiO_3$ for enhanced visible-light driven phtocatalytic hydrogen production, Opt. Quant. Electron. 53 (10) (2021) 589.
[88] T. Zhou, L. Wang, X. Huang, J. Unruangsri, H. Zhang, R. Wang, Q. Song, Q. Yang, W. Li, C. Wang, K. Takahashi, H. Xu, J. Guo, PEG-stabilized coaxial stacking of two-dimensional covalent organic frameworks for enhanced photocatalytic hydrogen evolution, Nat. Commun 12 (1) (2021) 3934.
[89] T. Xu, S. Wang, L. Li, X. Liu, Dual templated synthesis of tri-modal porous $SrTiO_3$/TiO_2@ carbon composites with enhanced photocatalytic activity, Appl. Catal., A 575 (2019) 132–141.
[90] T. Giannakopoulou, I. Papailias, N. Todorova, N. Boukos, Y. Liu, J. Yu, C. Trapalis, Tailoring the energy band gap and edges' potentials of g-C_3N_4/TiO_2 composite photocatalysts for NOx removal, Chem. Eng. J. 310 (2017) 571–580.
[91] M. Zhang, X. Bai, D. Liu, J. Wang, Y. Zhu, Enhanced catalytic activity of potassium-doped graphitic carbon nitride induced by lower valence position, Appl. Catal., B 164 (2015) 77–81.
[92] T. Šetinc, M. Spreitzer, D. Vengust, I. Jerman, D. Suvorov, Inherent defects in sol-precipitation/hydrothermally derived $SrTiO_3$ nanopowders, Ceram. Int. 39 (6) (2013) 6727–6734.
[93] F.A. Rabuffetti, H.-S. Kim, J.A. Enterkin, Y. Wang, C.H. Lanier, L.D. Marks, K. R. Poeppelmeier, P.C. Stair, Synthesis-Dependent First-Order Raman Scattering in $SrTiO_3$ Nanocubes at Room Temperature, Chem. Mater. 20 (17) (2008) 5628–5635.
[94] X. Chen, P. Tan, B. Zhou, H. Dong, J. Pan, X. Xiong, A green and facile strategy for preparation of novel and stable Cr-doped $SrTiO_3$/g-C_3N_4 hybrid nanocomposites with enhanced visible light photocatalytic activity, J. Alloys Compd. 647 (2015) 456–462.